Multiscale Registration of Realtime and Prior MRI Data for Image Guided Cardiac Interventions

Robert Xu*, Prashant Athavale, Adrian Nachman, and Graham A. Wright

***Abstract*—Recently, there is a growing interest in using magnetic resonance imaging (MRI) to guide interventional procedures due to its excellent soft tissue contrast and lack of ionizing radiation compared to traditional radiographic guidance. One of these applications is the use of MRI to guide radio-frequency (RF) ablation of anatomic substrates, within the left ventricle, responsible for ventricular tachycardia. However, different MRI acquisition schemes have significant tradeoffs between image quality and acquisition time. Guidance using high-quality pre-operative 3D MR images is limited in the case of cardiac interventions because the heart moves dynamically during the procedure. On the other hand, 2-D real-time MR images acquired during the intervention sacrifice image quality for shorter image acquisition time, leading to real-time positional updates of cardiac anatomy. Ideally, we wish to combine the advantages of live feedback from realtime images and accurate visualization of anatomical structures from pre-operative images. Therefore, to improve the MRI guidance capabilities for cardiac interventions, we describe a novel multi-scale rigid registration framework to correct for respiratory motion between the prior and realtime datasets. In the proposed approach, we use a weighted total variation (TV) flow algorithm to extract coarse-to-fine features from the input images and subsequently register the corresponding scales in a hierarchical manner. Registration experiments were performed with *in-vivo* human imaging data, and the target registration error achieved was 1.51 mm. Thus, the feasibility of motion correction in an interventional setting has been demonstrated, which may lead to significant improvements in the guidance of cardiac interventions.**

***Index Terms*—Image-guided cardiac interventions, magnetic resonance imaging, multiscale image registration.**

I. Introduction

CARDIOVASCULAR disease remains as one of the main causes of death in developed nations. Recent mortality data showed that cardiovascular disease accounted for over 800,000 deaths or 32.8% of all deaths in the United States [1]. One particular disease of interest in this study is ventricular tachycardia (VT), which is a cardiac arrhythmia caused by scarring from previous myocardial infarctions. The current curative treatment of VT requires the use of radio-frequency (RF) ablation to eliminate the anatomical substrate responsible for triggering the arrhythmia. To this end, image guided therapies have been proposed to guide mapping and ablation catheters to increase the accuracy and efficacy of cardiovascular procedures [2]–[9].

Traditionally, cardiovascular interventions are carried out under X-ray fluoroscopic guidance for diagnosis and treatment of arrhythmias. However, X-ray images have poor soft tissue contrast and it is therefore difficult to interpret the anatomical context from the images directly. The use of realtime magnetic resonance imaging (MRI) to guide cardiac interventions has also been proposed [2], [8], [10]. Although MRI has inherently superior soft tissue contrast compared to X-ray fluoroscopy, realtime MRI guidance also has its limitations. The increased acquisition frame rate is obtained at the expense of imaging quality and spatial coverage. Alternatively, the use of high resolution 3-D imaging roadmaps generated from computer tomography (CT) or MRI prior to the intervention have also been described [11]–[13]. However, one of the major limitations of guidance using high resolution roadmap images is that the images remain static, and do not account for patient respiratory motion during the interventional procedure. The amount of respiratory motion is subject dependent, and it has been shown that the movement can potentially exceed 16 mm [14], [15]. Therefore, patient respiratory motion can significantly reduce the targeting accuracy of RF ablation procedures.

In the ideal paradigm, we would like to combine the advantages of live feedback from realtime images, and accurate visualization of anatomical context from high resolution pre-procedural images. To this end, a number of registration studies have been reported in literature for aligning realtime and pre-procedural images in the context of surgical navigation and adaptive radiation therapy [16]–[19]. However, these studies focused on less mobile anatomical regions such as the prostate, rectum, lungs, as well as the head and neck areas. The registration problem for cardiac intervention is significantly more challenging due to the highly mobile nature of the heart [15]. Therefore, many cardiac image registration studies in the past have focused on offline cardiac analysis [20]–[24]. In a review of cardiac image registration methods [20], the authors discussed various methods for combining information from multiple cardiac image modalities for physiologic understanding and diagnostic purposes. Aladl *et al.* [21] proposed a registration method to align cardiac-gated SPECT and MR

Manuscript received January 14, 2014; revised April 4, 2014; accepted May 6, 2014. This work was supported by funding support from GE Healthcare and the Federal Development Agency of Canada. *Asterisk indicates corresponding author.*

*Robert Xu is with the Physical Sciences Platform, Sunnybrook Research Institute, Toronto, ON. M4N 3M5 Canada, and also with the Department of Medical Biophysics, University of Toronto, Toronto, ON. M5G 2M9 Canada (email: robert.xu@mail.utoronto.ca).

Prashant Athavale is with the Department of Mathematics, University of Toronto, Toronto, ON. M5S 1A1, Canada.

Adrian Nachman is with the Department of Mathematics, University of Toronto, Toronto, ON. M5S 1A1, Canada, and also with the Department of Electrical Engineering, University of Toronto, Toronto, ON. M5S 1A1, Canada.

Graham Wright is with the Physical Sciences Platform, Sunnybrook Research Institute, Toronto, ON. M4N 3M5 Canada, and also with the Department of Medical Biophysics, University of Toronto, Toronto, ON. M5G 2M9 Canada.

images for comparison of regional function and perfusion. Their algorithm requires the myocardium to be initially segmented in the cardiac MR images, which is subsequently registered to the gated SPECT image via maximization of mutual information (MI). Perperidis *et al.* [22] proposed a 4-D deformable registration algorithm to register 3-D MR imaging sequences from different subjects. Specifically, the free-form deformation model based on B-splines was used to separately correct for spatial and temporal misalignments. However, the reported computational time was approximately 1 hour. More recently, Shi *et al.* [24] proposed a non-rigid image registration method to estimate cardiac motion and evaluate regional volume and strain. In this case, a free-form deformation method was adopted and a spatially weighted normalized cross correlation (NCC) metric was chosen to utilize data from both tagged and untagged MR images. Although the above mentioned methods are suitable for offline cardiac function analysis, the extended computational times render them unsuitable for interventional applications.

Fewer studies have explored cardiac image registration for interventional purposes [5]–[7]. Huang *et al.* [5] proposed a two-step method to register realtime 3-D ultrasound images to high quality MR/CT images of the beating heart for diagnosis and surgical navigation. Excellent registration accuracy was achieved for both the phantom and human studies with an average target registration error of 2.59 mm and 1.76 mm respectively. However, this method requires an initial manual registration step, which is then automatically refined using a mutual information based registration method. Smolíková-Wachowiak *et al.* [6] presented an automatic registration method for aligning 2-D realtime MR images to 3-D pre-procedural MR images for interventional applications. They studied the effect of various imaging parameters on registration accuracy, and compared the efficacy of 2 different similarity metrics. In the optimal setting, excellent target registration errors were achieved (i.e. translation error was < 2.7 mm and rotation error was $< 3.6°$), but the capture range of the algorithm was only reported for up to 10 mm of initial misalignment between the realtime and prior imaging data. Ma *et al.* [7] proposed a feature-based algorithm to register 3-D echo to 3-D MR images for cardiac catheterization. They were able to achieve a mean error of 4.1 mm based on distance between anatomical and catheter landmarks. However, the algorithm initially requires a clinical expert to segment the left ventricle and identify points along the aorta in the echo image, which can take approximately 3 minutes. The subsequent automatic feature-based registration requires an additional 2 minutes to complete. Therefore, this algorithm is only used to compensate for bulk patient motion. Although the previous methods show promise, registration of cardiac images with potentially large misalignments due to respiratory motion remains challenging without manual user intervention.

In this paper, we propose a novel framework for registering pre-procedural 3-D MR images to 2-D realtime MR images to better utilize MR guidance for cardiac interventions within the left ventricle (LV). Specifically, a rigid transformation is applied to correct for respiratory motion induced misalignment between the prior and realtime datasets. The registration framework uses a novel edge preserving scale space filter based on weighted total variation (TV) flow to decompose each image into coarse and fine scales. Then, the realtime and prior images are registered in a coarse-to-fine manner using an edge sensitive distance metric, normalized gradient field (NGF) [25]. In the proposed approach, large structures or coarse scales in the images are registered first, before additional finer scale features are added to iteratively refine the resulting registration. It is shown that the proposed method is less likely to be trapped in a local minimum compared to other registration approaches, and is able to achieve a median target registration error of 1.51 mm *in-vivo*.

II. Methods

A. Image Acquisition

Cardiac images from 8 volunteers were acquired with a GE Signa HD 1.5T MRI scanner (GE Healthcare, Milwaukee, WI) using the manufacturer's 8-channel cardiac imaging coil. Two separate image acquisition protocols were used to obtain the images used in this study. For each subject, a pre-procedural high-resolution scan is first performed to acquire a prior roadmap image, followed by a low resolution realtime acquisition.

1) High Resolution Roadmap Acquisition: The prior roadmap image consists of a multi-slice 3-D volume acquisition, which encompassed the heart of the subject. These were standard clinical prescription slices parallel to the short axis (SAX) of the heart. A typical range of 11-13 slices were acquired to cover the entire left ventricle. For each slice, the subject was asked to hold their breath at end expiration, while the GE FIESTA pulse sequence was used to acquire images gated to mid-diastole. The acquired images had a field of view (FOV) = 350 mm, in-plane resolution = 1.3×1.3 mm^2, and slice thickness = 8 mm.

2) Low Resolution Realtime Acquisition: A fast spiral balanced steady state free precession (SSFP) sequence was used to acquire 2-D images in realtime at a frame rate of approximately 10 frames per second. The FOV was set to 350 mm, and the obtained resolution was $2.2\times2.2\times8$ mm^3. This set of data was acquired under free breathing. However, physiological data such as cardiac and respiratory gating information were also recorded using the electrocardiogram (ECG) trigger and respiratory bellows respectively. Furthermore, the geometry of the slice prescriptions mirrors the slices acquired in the high resolution roadmap images.

B. Multiscale Image Decomposition Based on TV Flow

Medical image registration is often a non-convex and time consuming optimization problem, which has many local minima. To tackle this challenging problem, multilevel or multiscale registration approaches have been proposed in the past [19], [26], [27] to register images of similar resolution levels or scales in a coarse-to-fine manner. These methods focus on first aligning large scale structures to obtain a good initial transformation before adding finer details to fine-tune the registration result. Similarly, we propose to use an edge preserving filter based on TV flow to decompose the prior

and realtime cardiac images into their natural coarse and fine scales, and then register the images in a hierarchical approach.

Decomposition of an image f can be considered as generating a smooth component u and a residual component $v = f - u$. In the variational approach described by Rudin, Osher, Fatemi (ROF) [28] the decomposition can be formulated in terms of the minimization problem as follows:

$$f = u_\lambda + v_\lambda, \;\; u_\lambda := \underset{u}{\operatorname{arginf}} \Big\{ \int_\Omega |\nabla u| + \lambda \int_\Omega |f-u|^2 \Big\}, \quad (1)$$

where the $\Omega \subset \mathbb{R}^2$ denotes the imaging domain, and the minimizer u_λ is a smooth version of f with a fixed scale $1/\lambda$. The smooth image u_λ is constrained to be in the space of finite total variation ($\int_\Omega |\nabla u_\lambda| < \infty$), and the residual v_λ is in the mathematical space L^2, the space of square integrable functions.

In this study, we consider a different version of the minimization problem compared to (1), shown as follows:

$$f = u_\lambda + v_\lambda, \;\; u_\lambda := \underset{u}{\operatorname{arginf}} \Big\{ \int_\Omega \alpha\, |\nabla u| + \lambda \int_\Omega |f-u|^2 \Big\}, \quad (2)$$

where $\alpha \equiv \alpha(x)$ is a spatially varying weight that is independent of u, but depends on the given data f. Motivated by [29], we now extend this minimization problem (2) to produce a multiscale decomposition. To this effect, the multiscale decomposition algorithm can generate a multiscale family $\{u_\lambda, v_\lambda\}$ where λ denotes an algorithm specific scale parameter. First, we consider the decomposition of the original f into $f = u_{\lambda_0} + v_{\lambda_0}$ using a large parameter $\lambda = \lambda_0$. Then, we decompose $u_{\lambda_0} = u_{\lambda_1} + v_{\lambda_1}$, with $\lambda_1 < \lambda_0$. This process is repeated iteratively with $\lambda_{i+1} < \lambda_i$ to obtain successively smoothed versions $u_{\lambda_{i+1}}$ with coarser scale features, thus producing a nonlinear multiscale decomposition as follows:

$$\begin{aligned} f &= u_{\lambda_0} + v_{\lambda_0} \\ &= u_{\lambda_1} + v_{\lambda_1} + v_{\lambda_0} \\ &= \cdots \\ &= u_{\lambda_N} + \sum_{i=0}^{N} v_{\lambda_i}. \end{aligned} \quad (3)$$

Here we note that this multiscale decomposition is equivalent to removing noise and oscillations at certain scales, thus smoothing the image at each iteration. This approach differs from [29], where the algorithm started with a coarse image, and finer details were successively added at dyadic scales. We also distinguish the proposed approach from our earlier work [30], where we introduced a similar decomposition, but the TV seminorm $\int_\Omega |\nabla u|$ was not weighted by the spatially varying α.

Using the Euler-Lagrange differential equation [31] of (2), and rearranging equation (3) gives us:

$$u_{\lambda_N} = f - \sum_{i=0}^{N} v_{\lambda_i} = f + \sum_{i=0}^{N} \frac{1}{2\lambda_i} \operatorname{div}\left(\frac{\alpha \nabla u_{\lambda_i}}{|\nabla u_{\lambda_i}|} \right), \quad (4)$$

where $\{\lambda_i\}_{i=1}^N$ is a monotonically decreasing sequence. Considering λ_i as samples from a real valued monotonically decreasing function $\lambda(t)$ motivates the following integro-differential equation:

$$u(x,t) = f(x) + \int_0^t \frac{1}{2\lambda(s)} \operatorname{div}\Big(\frac{\alpha \nabla u(x,s)}{|\nabla u(x,s)|} \Big)\, ds. \quad (5)$$

As time t increases, the image $u(\cdot, t)$ becomes successively smoother versions of the original image f. Differentiating (5) formally with respect to t yields:

$$\frac{\partial u}{\partial t} = \mu(t) \operatorname{div}\Big(\frac{\alpha \nabla u}{|\nabla u|} \Big), \quad (6)$$

where $u(t=0) := f$ with Neumann boundary condition, and $\mu(t) = 1/2\lambda(t)$ is the speed function, which is set to $\mu(t) = 1.1^t$. We consider equation (6) as multiscale weighted TV flow (see Appendix for numerical solution to this equation), which is closely related to total variation flow [32].

To enhance the edge-preserving nature of the flow in (6), we choose the spatial weight α as follows:

$$\alpha(x) = \frac{1}{\sqrt{1 + |\nabla (G_\sigma * f)(x)|^2 / \beta^2}} \quad (7)$$

where G_σ is a Gaussian kernel with a small standard deviation σ, and $\beta \in \mathbb{R}$, which is chosen such that $\alpha(x)$ attains small values at prominent edges in the image. Small values of β close to 0 enhance the edge preserving nature of the weighted TV flow, but could also preserve noise artifacts that have sharp transitions in intensity. In contrast, as the value of β increases, $\alpha(x)$ approaches unity, which reduces the constraint on edge smoothing in the weighted TV flow. For the experiments in this paper, β was set to 0.07 to emphasize the preservation of prominent edges belonging to anatomical boundaries.

We observe that the weighted TV flow produces a multiscale representation of a given image f (see Fig. 1). Theoretically, this flow differs from the well known edge preserving Perona-Malik equation, which is defined in [33] as:

$$\frac{\partial u}{\partial t} = \operatorname{div}\Big(g(|\nabla u|) \nabla u \Big). \quad (8)$$

In fact, if we treat the Perona-Malik equation as the solution to a minimization problem [34], and set $g(s) = \frac{1}{1+s^2/\kappa^2}$ as proposed in [33], then (8) can be viewed as a flow corresponding to minimization of the following functional:

$$J_{PM}(u) = \frac{\kappa^2}{2} \int_\Omega \ln\Big(1 + \frac{|\nabla u|^2}{\kappa^2} \Big)\, dx, \quad (9)$$

which is a fundamentally different minimization problem compared to our consideration in (2). Moreover, the weight α in (6) is a function of the original data f rather than u, which can help to preserve prominent edges at coarser scales. This stems from the fact that f is a constant, whereas u is smoothed over time.

C. Hiearchical Multiscale Image Registration

Mathematically, registration of a template image f to a reference image g can be posed as an optimization problem as follows:

$$\arg\min_w \big\{ \mathcal{D}(f[w], g) \big\}, \quad (10)$$

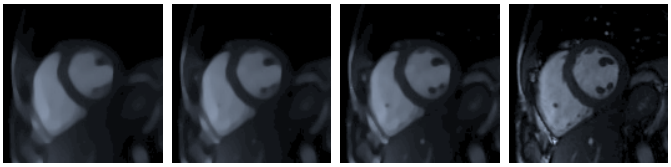

Fig. 1. Image decomposition using weighted TV flow. Images from left to right show images with coarse to increasingly fine scale features. This corresponds to decreasing values of the artificial time t in (5).

where $w : \mathbb{R}^3 \rightarrow \mathbb{R}^3$ is a geometric transformation, and $\mathcal{D}$ measures the distance between the transformed template image $f[w]$ and the reference image g. In this study, the geometric transformation chosen is a rigid-body transformation, because the acquired images are gated to the same cardiac phase. However, in general, w can be any arbitrary transformation. The distance measure $\mathcal{D}$ is chosen to be the normalized gradient field measure $\mathcal{D}_{\mathcal{NGF}}$, which is defined as [25]:

$$\mathcal{D}_{\mathcal{NGF}} = -\frac{1}{2}\int_{\Omega} \langle \hat{\mathbf{n}}(f,x), \hat{\mathbf{n}}(g,x)\rangle^2 dx \ , \qquad \hat{\mathbf{n}}(I,x) := \frac{\nabla I(x)}{\|\nabla I(x)\|_{\varepsilon}} \ , \tag{11}$$

where $\langle \cdot, \cdot \rangle$ denotes the vector dot product, and $\hat{\mathbf{n}}$ represents the normalized gradient of the image. For $x \in \mathbb{R}^m$, $\|x\|_{\varepsilon} = \sqrt{\sum_{k=1}^{m} x_k^2 + \varepsilon^2}$ and $\nabla I := (\partial_1 I, \cdots, \partial_m I)$. The parameter ε is a regularizing term that minimizes the effects of small gradients due to noise, and is automatically set as follows:

$$\varepsilon = \frac{\eta}{V}\int_{\Omega} |\nabla I(x)| dx, \tag{12}$$

where η is the estimated noise level in the image, and V is the volume of the domain.[1]

NGF is an alternative to MI based registration metrics, and is derived from the observation that if two images are similar, then many intensity changes should occur at the same location. The motivation for using this edge sensitive metric is that we wish to align spatial features such as contours and boundaries, which often denote transitions between tissue types.

The optimization in (10) is achieved via the proposed multiscale registration framework illustrated in Fig. 2, and the simplex minimization algorithm [35] was used at each scale. Smoothed template $u_f(\cdot, t)$ and reference $u_g(\cdot, t)$ images are obtained via weighted TV flow (6), where $t_0 > t_1 ... > t_N$. Then, the coarse scale image pairs $u_f(\cdot, t_0)$ and $u_g(\cdot, t_0)$ are subsampled (denoted by operator $D_{\downarrow}$) by a factor of 2^N before registration; the resulting transformation is used as the initialization for the image pair with finer scales. This process is repeated for N additional levels, where the subsampling factor is reduced by 2 at each level, until the final registration result is obtained. In this study, the number of levels $N = 3$.

[1]In this paper, the value of ε was approximately 0.01 and 0.04 for the prior and realtime images respectively, assuming image intensity range is normalized to [0, 1].

III. Experiments and Results

Validation of the proposed multiscale registration framework was performed for prior roadmap and realtime MR images acquired from 8 volunteers at the Sunnybrook Health Sciences Centre (Toronto, ON). Specifically, two experimental protocols were adopted to quantitatively evaluate the registration accuracy of the proposed registration technique. One is a controlled experiment, where the ground truth registration transformations were known, and the registration accuracy was evaluated based on the proposed framework's ability to recover the known transformations. In the second experiment, the realtime images were acquired during free breathing, and the ground truth registration parameters were unknown. In this case, the registration accuracy was estimated via two different evaluation metrics. In the first evaluation criterion, the Dice similarity coefficient (DSC) [36] was computed between the manually segmented LV endocardium boundary from a realtime image and the corresponding segmentation from a registered prior image. During the second evaluation, the in-plane distance between visible landmarks from prior and realtime images after image registration was computed. Details are presented in the following sections.

A. Controlled Registration Experiment Setting

To quantitatively evaluate the accuracy of the proposed framework, a controlled study was performed. The prior images were acquired during end-expiration breath-holds and retrospectively gated to the mid-diastolic cardiac phase. On the other hand, the acquired realtime images were retrospectively gated to the same mid-diastolic cardiac phase and end-expiration respiratory phase. Moreover, the same geometric slice prescriptions were used for both the prior and realtime scans, which were acquired a few minutes apart during the same scan session. During the session, the volunteer subjects were securely strapped down by the cardiac imaging coil and did not move out of the MR bore between the two scans. Therefore, in this controlled study, the prior and realtime images were optimally aligned and considered as ground truths for the ensuing registration. Subsequently, the spatial locations of landmarks within the heart such as the LV apex, papillary muscles, and aortic valve annulus were identified, and their (x, y, z) coordinates were recorded from the aligned images.

Next, a known transformation $\omega_d = \langle \theta_x, \theta_y, \theta_z, t_x, t_y, t_z \rangle$ consisting of rotations and translations was applied to the prior roadmap image, causing a mean displacement equal to a predefined value d for the selected landmarks. The rotation and translation parameters were randomly generated with independent and identically uniform distributions. For each predefined value of d = 5, 10, 15, 20 mm, 100 transformations were generated. Thus, 400 transformations were generated for each of the 8 volunteer subjects, creating 3200 registration cases in total. Subsequently, the misaligned 3-D prior roadmap image f and a 2-D realtime image g were supplied to the proposed registration framework (Fig. 2) to attempt to recover the known transformation. During this process, we also evaluated the effect of using different image decomposition schemes or registration distance metrics. Since the ground

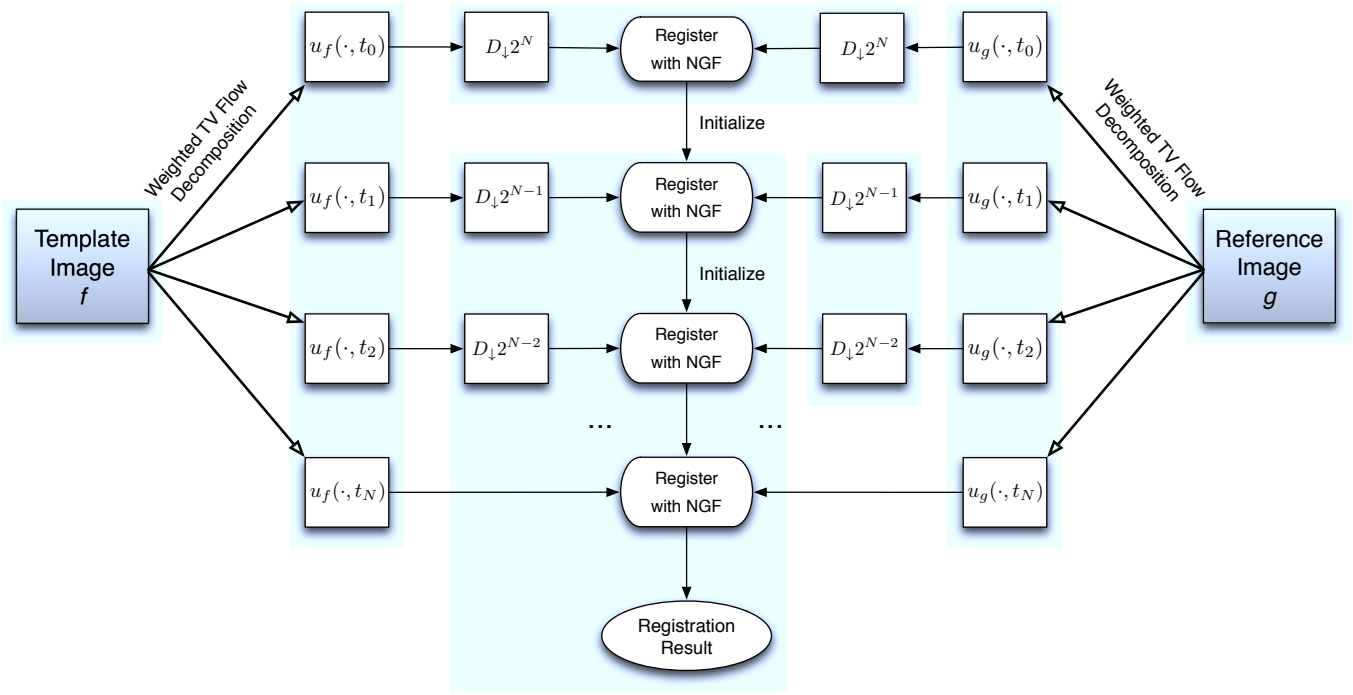

Fig. 2. Multiscale TV flow registration framework using the normalized gradient field metric. Both the template f and reference g images are decomposed into coarse and fine scale images corresponding to decreasing values of $t : t_0 > t_1 > ... > t_N$. The extracted scale images are then down-sampled and registered iteratively in a coarse-to-fine manner.

truth transformation is known, the target registration error (TRE) can be defined as:

$$\mathrm{TRE} = \frac{1}{M}\sum_{j=1}^{M} \| L\left(f[\omega_r], j\right) - L\left(g, j\right) \|_{l^2} \qquad (13)$$

where $\omega_r : \mathbb{R}^3 \rightarrow \mathbb{R}^3$ is the recovered geometric transformation, and M denotes the number of landmarks. The corresponding anatomical landmark locations of the transformed prior and realtime images are represented by $L\left(f[\omega_r], j\right)$ and $L\left(g, j\right)$ respectively, where $j = 1, ..., M$. Finally, $\| \cdot \|_{l^2}$ represents the Euclidean norm.

B. Controlled Registration Experiment Results

The controlled experimental results obtained using the proposed registration framework are summarized in Fig. 3a. In the proposed approach, both the prior and realtime data were decomposed using the weighted TV flow algorithm, and subsequently registered via minimizing the NGF metric. For comparison, the registration results using the NGF metric with a Perona-Malik hierarchical decomposition scheme (Fig. 3b) and a Gaussian hierarchical decomposition scheme (Fig. 3c) are also presented. Specifically, the same registration framework shown in Fig. 2 was applied, but the weighted TV flow decomposition step was replaced by the Perona-Malik anisotropic diffusion filter [33] in the former approach and a Gaussian filter in the latter approach. Box-and-whisker plots were used to describe the results, since the errors were not normally distributed, as confirmed by the Anderson-Darling test [37]. The median TREs for all 3 registration approaches were below the desired clinical accuracy of 5 mm (i.e. the dotted line in Fig. 3) for initial misalignments of up to 20 mm. However, it was observed that lower upper bounds of the TREs were achieved with the proposed weighted TV flow decomposition scheme. Specifically, when we combined the registration results for all 4 initial misalignment distances, the median TREs were 1.28, 1.31, and 1.30 mm for the weighted TV flow, Perona-Malik, and Gaussian approaches respectively. However, the TREs at the 90th percentile were 4.27, 6.51, and 9.82 mm for the weighted TV flow, Perona-Malik, and Gaussian approaches respectively.

Since the TRE distributions were not normally distributed and displayed positive skew, the non-parametric Wilcoxon signed-rank test [38] was used to test for statistical significance between the results of the different registration approaches. A paired difference test was chosen because, in each registration trial, the different registration approaches all attempted to correct for the same misalignment generated by a known transformation. Using the Wilcoxon signed-rank test [38], we found at the 1% significance level (i.e. $p < 0.01$) that lower target registration errors were achieved using the weighted TV flow approach compared to Perona-Malik ($p < 0.01$) and Gaussian ($p < 0.01$) pre-processing. The improvement in registration accuracy may be attributed to the fact that the NGF measure is sensitive to edge information, and the weighted TV flow decomposition algorithm is better able to preserve the prominent edges during its iterative filtering process.

Furthermore, we also compared the registration results obtained via the proposed registration framework using NGF as the registration metric with other well established distance

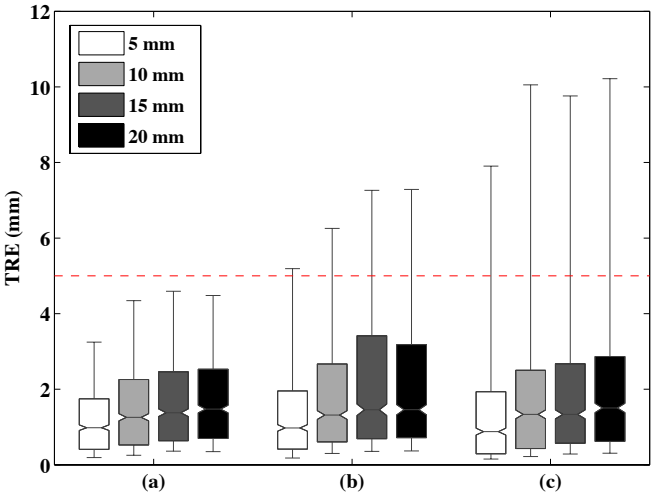

Fig. 3. Comparison of registration results using the NGF distance metric and different image pre-processing schemes. Registration accuracy was evaluated for aligning prior and realtime images (a) with weighted TV flow pre-processing, (b) with the Perona-Malik anisotropic diffusion filter pre-processing, and (c) with Gaussian pre-processing. For each approach, there are 4 box-and-whisker plots, which illustrates the median (notch), interquartile range (box), and 10th and 90th percentiles (whiskers) of the TRE after registration for all the volunteers with an initial known misalignment of d = 5, 10, 15, and 20 mm respectively.

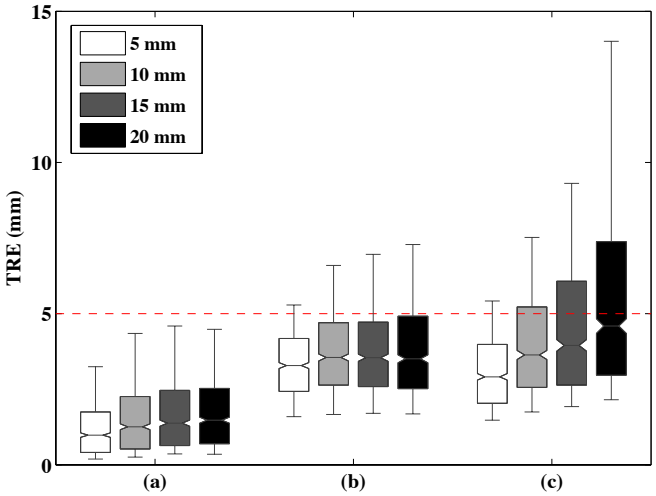

Fig. 4. Comparison of registration results using the proposed weighted TV flow registration framework with different distance metrics. Registration accuracy was evaluated for the (a) NGF metric, (b) NCC metric, and (c) the MI metric. For each approach, there are 4 box-and-whisker plots, which illustrates the median (notch), interquartile range (box), and 10th and 90th percentiles (whiskers) of the TRE after registration for all the volunteers with an initial known misalignment of d = 5, 10, 15, 20 mm respectively.

metrics such as NCC and MI. Specifically, the weighted TV flow algorithm was first used to extract the different scale features from the prior and realtime images. Then, the registration was performed using the NCC or MI metric instead of NGF. The registration results are shown in Fig. 4. Again, the Wilcoxon signed-rank test was used, and we observe that registrations with NGF achieved significantly lower TREs compared to registration with NCC ($p < 0.01$) and MI ($p < 0.01$).

Overall, it was observed that the lowest median target registration error of 1.28 mm was achieved using the combination of NGF as the distance metric, and weighted TV flow as the image decomposition method. An example of a successful registration using the proposed method is shown in Fig. 5. Note that the difference image between the prior and realtime image before registration (Fig. 5c) shows distinct anatomical structures in the region of interest as highlighted by the circle centred around the LV. On the other hand, the difference image after registration (Fig. 5f) shows more uniform intensity variations within the region of interest, which is due to the inherent difference in the contrast mechanisms of the two acquisitions rather than structural misalignment.

C. Free Breathing Registration Experiment Setting

To evaluate the proposed registration framework in a more clinically relevant scenario, the volunteers were asked to breathe normally during this experiment, while the realtime images were continuously acquired. The acquired prior roadmap images still consisted of a stack of slices that covered the entire LV, and were gated to mid-diastole and end-expiration as before. In contrast, the acquired realtime images consisted of a single imaging slice within the LV, and were

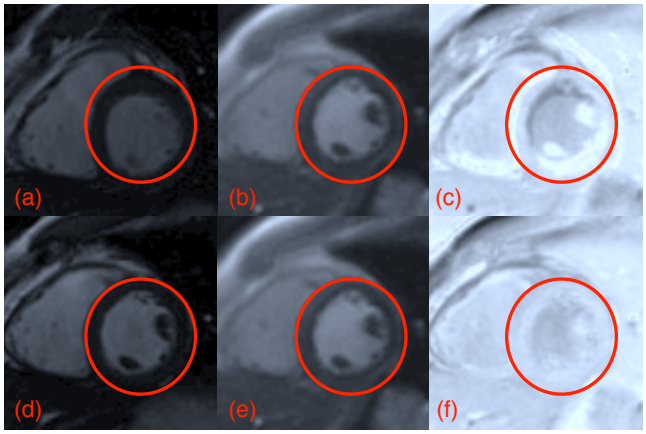

Fig. 5. Controlled registration experiment between prior 3-D volume and realtime 2-D image. (a) Initially misaligned imaging slice from the prior 3-D volume; (b) reference 2-D realtime image; (c) the absolute difference image between images (a) and (b). (d) The registered imaging slice from the prior 3-D volume; (e) reference 2-D realtime image; (f) the absolute difference image between the registered images (d) and (e).

only retrospectively gated to the same mid-diastolic cardiac phase. Since the realtime images were acquired continuously in time, and were not gated to end-expiration, they could be in any arbitrary respiratory phase. Moreover, due to the difference in respiratory phase between the two datasets, the ground truth alignment is unknown. A total of 179 registration cases were performed, which included registrations between 9-29 realtime single slice 2-D images from each of the 8 subjects and their corresponding 3-D prior roadmap images.

To correct for the respiratory motion induced misalignment, we used the proposed registration framework with the NGF metric to register the prior volume to the realtime image. The choice of the NGF metric was based on results of the

previous controlled registration experiment, where registration using the NGF metric demonstrated higher accuracy compared to NCC and MI. In terms of image decomposition schemes, we compared the registration accuracy achieved with the proposed weighted TV flow algorithm to the Perona-Malik pre-processing method, and Gaussian pre-processing of the prior and realtime images.

In this experiment, the registration accuracy was estimated via the DSC and the in-plane target registration error. DSC is defined as [36]:

$$\mathrm{DSC}(M_{prior}, M_{realtime}) = \frac{2|M_{prior} \cap M_{realtime}|}{|M_{prior}| + |M_{realtime}|}, \quad (14)$$

where M_{prior} and $M_{realtime}$ represents the manual segmentation masks of the left ventricle endocardial border from the prior and realtime images respectively. The DSC measure is illustrated in Fig. 6, where the overlap between the contours of the LV endocardial border in the prior and realtime image is shown in Fig. 6b for the initially misaligned case (DSC = 82.9%), and Fig. 6d for the motion corrected case using the proposed registration method (DSC = 95.2%). The higher DSC indicates improved image alignment, which is confirmed by visual observation. Alternatively, the in-plane TRE can also be measured as an indicator of registration accuracy. Equation (13) can be used to measure the average distance between visible landmarks (e.g. papillary muscles) in the prior and realtime datasets from the intersecting imaging plane after registration.

The manual segmentations and landmark identifications were performed by two experts. Each observer was asked to perform the segmentation and landmark identification tasks for both the realtime and prior images, using a custom MATLAB application. Each task was performed in two separate sessions, where each observer was not aware of the other's results. The average DSC measure between the two experts' segmentations was 97.4%, while the average distance between the identified landmarks was 0.80 mm.

D. Free Breathing Registration Experiment Results

The free breathing registration experiment results for DSC and in-plane TRE are summarized in Table I and Table II respectively. As a baseline reference, we computed the median DSC and in-plane TRE values for the prior and realtime datasets before registration was applied. As expected, a relatively low DSC value (88.0%) and a high in-plane TRE (4.35 mm) were obtained due to misalignments caused by respiratory motion. Subsequently, a comparison of the 3 different registration approaches showed that the highest median DSC value (95.5 %) and lowest median in-plane TRE (1.51 mm) were achieved using the proposed method of applying weighted TV flow as the pre-processing scheme with NGF as the registration distance metric. Again, using the Wilcoxon signed-rank test, it was observed that the proposed method achieved higher DSC values compared to Perona-Malik ($p < 0.01$) and Gaussian ($p < 0.01$) approaches. Similarly, the proposed method obtained lower in-plane TREs compared to Perona-Malik ($p < 0.01$) and Gaussian ($p < 0.01$) approaches.

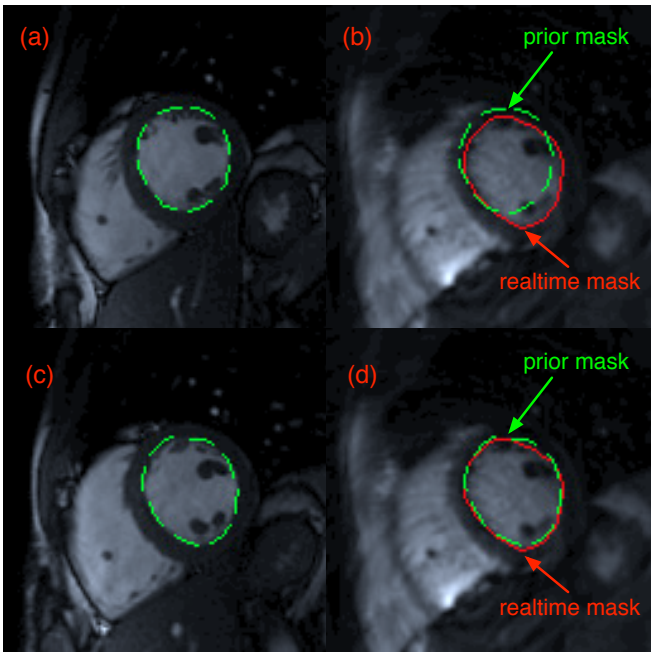

Fig. 6. Dice similarity coefficient measure. (a) Extracted 2-D slice from the prior 3-D volume before registration and the corresponding manual segmentation of the LV endocardium (dashed line). (b) The direct overlay of the prior mask from (a) is shown together with the contour of the LV endocardium (solid line) in the realtime image. (c) Registered prior image with corresponding LV contour (dashed line). (d) Overlay of the registered prior contour from (c) and contour of the LV (solid line) in the realtime image.

TABLE I
FREE BREATHING REGISTRATION EVALUATION FOR DIFFERENT IMAGE PRE-PROCESSING SCHEMES. THE MEDIAN, 10TH PERCENTILE, 90TH PERCENTILE, AND INTERQUARTILE RANGE (IQR) VALUES FOR DSC MEASUREMENTS ARE SHOWN FOR N=179 PAIRS OF REALTIME AND PRIOR IMAGES.

	DSC (%)			
Registration Method	Median	10th Percentile	90th Percentile	IQR
No Registration	88.0	69.6	93.8	8.20
NGF + Gaussian	95.0	92.1	96.8	2.40
NGF + Perona-Malik	95.1	92.1	97.1	2.39
NGF + weighted TV flow	95.5	92.9	97.1	1.93

TABLE II
FREE BREATHING REGISTRATION EVALUATION FOR DIFFERENT IMAGE PRE-PROCESSING SCHEMES. THE MEDIAN, 10TH PERCENTILE, 90TH PERCENTILE, AND INTERQUARTILE RANGE (IQR) VALUES FOR IN-PLANE TRE MEASUREMENTS ARE SHOWN FOR N=179 PAIRS OF REALTIME AND PRIOR IMAGES.

	TRE (mm)			
Registration Method	Median	10th Percentile	90th Percentile	IQR
No Registration	4.35	2.30	11.54	3.25
NGF + Gaussian	1.70	0.88	3.77	1.22
NGF + Perona-Malik	1.63	0.89	3.34	1.33
NGF + weighted TV flow	1.51	0.85	3.28	1.20

E. Computational Time

In our experiments, the pre-processing time associated with weighted TV flow decomposition was approximately 3.08 seconds for a multi-slice prior dataset of size $256 \times 256 \times 12$, and 0.27 seconds for a single 2-D realtime image of size 256×256. The subsequent coarse-to-fine registration process for a pair of prior and realtime images required 29.17 ± 3.02 s to complete when the NGF distance metric was used, whereas the computational time was 27.94 ± 3.38 s and 30.46 ± 4.25 s for registrations with the NCC or MI distance metric respectively. Thus, the computational complexity of NGF is slightly higher than NCC, but lower than MI. Currently, the overall registration framework is implemented using unoptimized MATLAB code and evaluated on a MacBook Pro laptop with 2.66 GHz Core i7 processor and 4GB of RAM.

IV. Discussions

A. Distance Metric Evaluation

In the previous section, we demonstrated that the proposed registration method using the weighted TV flow algorithm and NGF metric was effective for aligning prior roadmap and realtime MR images. In fact, in our experiments the NGF metric outperformed traditional NCC and MI metrics. This may be explained by analyzing the cost function curves for each metric, which are visualized in Fig. 7. These cost curves were generated from a pair of initially aligned prior and realtime images by applying small rotations and translations to the prior volume and computing the corresponding distance metric values.[2] For the plots in Fig. 7, no pre-processing techniques were applied to the prior and realtime images. For each metric, there are 6 cost curve plots, corresponding to rotations and translations in 3-D. In each plot, one registration parameter is varied near the vicinity of the correct registration value, while the other parameters are kept constant at the correct registration values.

We observe for the NCC plots (Fig. 7a) that the cost curves are smoothly varying, and have very few local minima. However, the cost functions have a relatively broad minimum, and the global minimum for some registration parameters are shifted from the correct solution at the 0 offset. This suggests that registrations using the NCC metric should be robust and generally converge to the near vicinity of the correct solution, but will not obtain a very accurate registration. This is evident in the controlled registration experiment (Fig. 4b), where the obtained median TREs were relatively stable in the range of 3-4 mm regardless of the magnitude of the initial misalignment. In contrast, the MI cost curves (Fig. 7b) are very noisy, have many local minima, and the global minima from the different cost curve plots are also shifted from the correct solution at the 0 offset. Therefore, registrations using the MI distance metric are prone to be trapped at a local minimum, which can be far away from the correct registration. This is demonstrated in the controlled registration experimental results (Fig. 4b), where the median and upper bounds of the TRE for MI registrations increased significantly as the magnitude of the initial misalignment increased. Finally, for the NGF cost curves (Fig. 7c), it is shown that all of the curves except for the translation parameter in the y-direction of the SAX imaging plane (i.e. T_y) have a sharp global minimum at the correct registration. This offset in T_y could be due to the presence of imaging artifacts, which leads to detection and alignment of false edges. However, this error is minimal, as the NGF cost function is still dominated by prominent edges corresponding to true anatomical boundaries. Although the cost curves for NGF are not as smooth as the NCC curves, the global minima are more sharply defined and closer to the correct solution. Also, the number of local minima in the NGF cost curves is significantly less compared to the MI curves. Accordingly, the median TREs achieved in the controlled experiment for registrations with the NGF metric (Fig. 4) were lower than both NCC and MI.

[2]Note that the cost functions have all been normalized to [0 1].

B. Weighted TV Flow Enhancement

Further improvements to the registration accuracy were observed in both the controlled and free breathing registration experiments after the weighted TV flow image decomposition algorithm was applied to the input images. The fact that the weighted TV flow algorithm behaves as an edge preserving filter is particularly useful when applied in conjunction with an edge sensitive metric such as NGF, since the latter relies on identification and alignment of prominent edges in the images. Additionally, the coarse-to-fine scale registration framework using weighted TV flow can improve the registration robustness by initially removing fine-scale features, leading to a reduced number of local minima in the cost function. These characteristics are evident in the NGF cost curves shown in Fig. 8, where the input prior and realtime images have been pre-processed using weighted TV flow. We see that all 6 cost curve plots have their global minimum close to the zero offset position, and the cost curves for translations T_x and T_y are smoother compared to the plot produced in Fig. 7c. Thus, the combination of weighted TV flow and NGF produced the best registration results in both the controlled and free breathing experiments of this study.

C. Limitations and Future Works

In the experiments of this study, a rigid-body transformation model was chosen to correct for respiratory motion induced misalignment between the realtime and prior images. It was shown in [39], that a rigid-body transformation is a reasonable model to describe respiratory motion of the LV, provided that ECG gating is used to align the corresponding images in the same cardiac phase. The same rigid-body transformation model was also adopted for image registration studies in [5], [6], [21], [40], when ECG gating was applied. Alternatively, non-rigid transformation models could have been used, which includes affine and free-form deformable transformations. The additional degrees of freedom introduced in non-rigid transformations may be able to describe the motion of the heart with increased accuracy. However, from an optimization perspective, the additional degrees of freedom may also lead

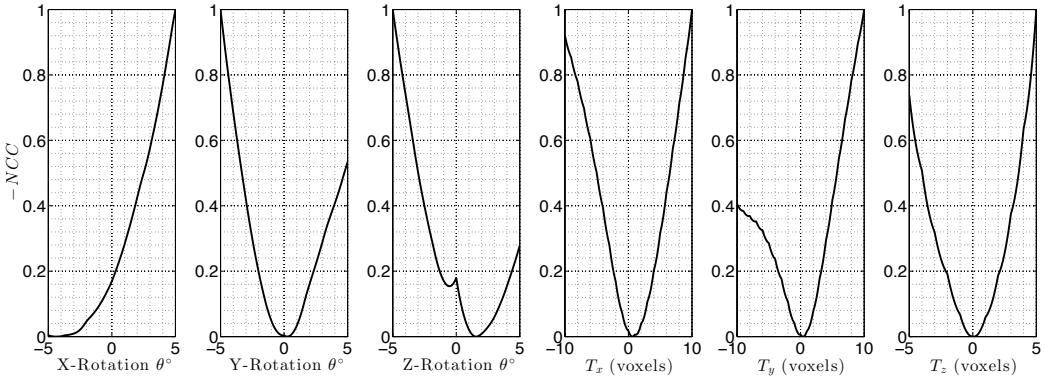

(a)

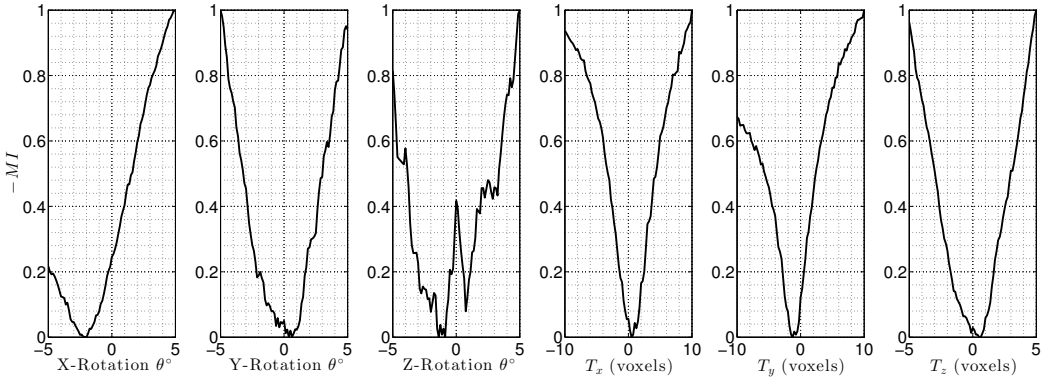

(b)

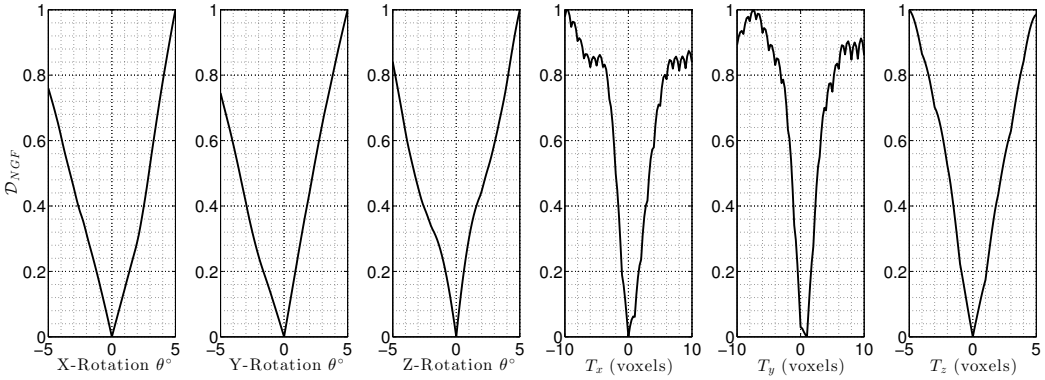

(c)

Fig. 7. Cost curves for the different distance metrics. Rotation and translation offsets were applied to a prior image to move it out of alignment with a paired realtime image. For each transformation, corresponding distance metric values were computed for the (a) NCC metric, (b) MI metric, and (c) NGF metric.

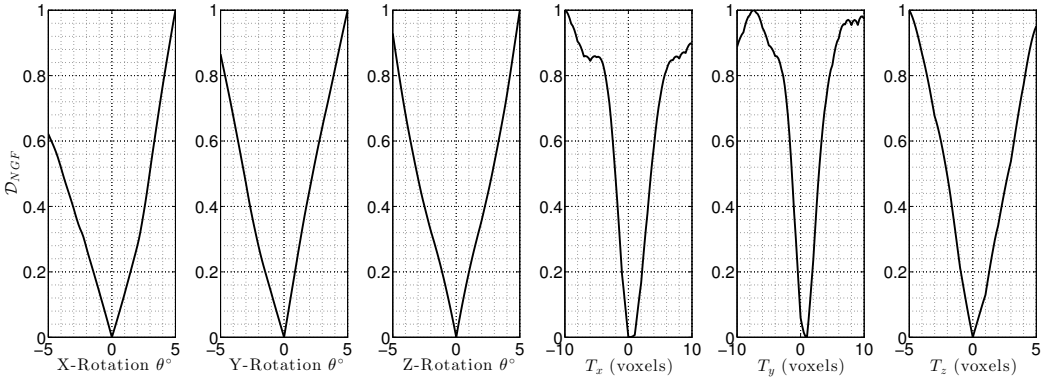

Fig. 8. NGF cost curves after pre-processing the aligned prior and realtime images with weighted TV flow for $t = 0.25$. Rotation and translation offsets were applied to the filtered prior image to move it out of alignment with the filtered realtime image, and corresponding NGF metric values were computed.

to convergence to undesirable local minima due to the non-convex nature of the optimization problem. Moreover, the use of non-rigid registration will also significantly increase the computational time. These are potentially significant drawbacks, as the intended application in this study is for realtime MR intervention. Therefore, a rigid-body motion model was adopted in the current study.

As part of the future work, we are planning to implement the proposed registration framework using graphics processing unit (GPU) acceleration methods to further reduce the overall computational time. We believe that near realtime (i.e. $<$1 s) registration can be achieved after optimization [41]. However, in the scenario where the registration speed is still insufficient, then the additional latency may potentially be corrected by using a motion modelling approach [42]. Specifically, the real-time registration method would be used in an initial calibration stage to create a dynamic motion model, which is then updated periodically as new registration parameters are obtained. Subsequently, the model should be able to predict and correct for motion misalignments with minimal latency.

V. Conclusion

In this paper, a novel registration framework consisting of a multiscale edge-preserving filter and an edge sensitive registration metric was proposed for aligning realtime and prior roadmap images for the purpose of guiding MRI based cardiac interventions. This method was validated in a controlled experiment with known ground truth, as well as in a free breathing experiment using data acquired from 8 human subjects. In the controlled study, we achieved a median target registration error of 1.28 mm for initial misalignments of up to 20 mm. Alternatively, in the free breathing experiment, the proposed method achieved a median in-plane target registration error of 1.51 mm. Thus, this proof of concept study showed that it is feasible to correct for respiratory motion induced errors to within the accuracy requirement of our target application. This combination of motion corrected roadmaps with realtime imaging should lead to significant improvement in the guidance of cardiac interventions.

Appendix
Numerical Scheme for Weighted TV Flow

In this section we provide the details of a fast semi-implicit numerical scheme for solving the weighted TV flow (6). Let h and τ be the space and time discretization steps respectively. We denote the value of the function u at the location $(x, y) \equiv (ih, jh)$, and at time $t = n\tau$ by $u^n_{i,j}$. With this notation we have the following discretization for the right hand side of (6)

$$\begin{aligned}
&\mu\Big(D_{-x}\Big[\frac{\alpha_{i,j}D_{+x}u_{i,j}}{\sqrt{\epsilon^2+(D_{+x}u_{i,j})^2+(D_{0y}u_{i,j})^2}}\Big]\\
&\quad + D_{-y}\Big[\frac{\alpha_{i,j}D_{+y}u_{i,j}}{\sqrt{\epsilon^2+(D_{0x}u_{i,j})^2+(D_{+y}u_{i,j})^2}}\Big]\Big)\\
&= \frac{\mu}{h^2}\Big[\frac{\alpha_{i,j}(u_{i+1,j}-u_{i,j})}{\sqrt{\epsilon^2+(D_{+x}u_{i,j})^2+(D_{0y}u_{i,j})^2}}\\
&\quad - \frac{\alpha_{i-1,j}(u_{i,j}-u_{i-1,j})}{\sqrt{\epsilon^2+(D_{-x}u_{i,j})^2+(D_{0y}u_{i-1,j})^2}}\\
&\quad + \frac{\alpha_{i,j}(u_{i,j+1}-u_{i,j})}{\sqrt{\epsilon^2+(D_{0x}u_{i,j})^2+(D_{+y}u_{i,j})^2}}\\
&\quad - \frac{\alpha_{i,j-1}(u_{i,j}-u_{i,j-1})}{\sqrt{\epsilon^2+(D_{0x}u_{i,j-1})^2+(D_{-y}u_{i,j})^2}}\Big],
\end{aligned}$$

where, D_+, D_-, D_0 denote the forward, backward and central difference schemes, respectively. We use the following notation

$$\begin{aligned}
C_E &= \frac{1}{\sqrt{\epsilon^2+(D_{+x}u^n_{i,j})^2+(D_{0y}u^n_{i,j})^2}}\\
C_W &= \frac{1}{\sqrt{\epsilon^2+(D_{-x}u^n_{i,j})^2+(D_{0y}u^n_{i-1,j})^2}}\\
C_S &= \frac{1}{\sqrt{\epsilon^2+(D_{0x}u^n_{i,j})^2+(D_{+y}u^n_{i,j})^2}}\\
C_N &= \frac{1}{\sqrt{\epsilon^2+(D_{0x}u^n_{i,j-1})^2+(D_{-y}u^n_{i,j})^2}}.
\end{aligned}$$

Thus, we get the following discretization for (6)

$$\begin{aligned}
&\frac{u^{n+1}_{i,j}-u^n_{i,j}}{\tau} =\\
&\frac{\mu^{n+1}}{h^2}[C_E\alpha_{i,j}u^n_{i+1,j}+C_W\alpha_{i-1,j}u^n_{i-1,j}+C_S\alpha_{i,j}u^n_{i,j+1}\\
&+C_N\alpha_{i,j-1}u^n_{i,j-1}\\
&-(C_E\alpha_{i,j}+C_W\alpha_{i-1,j}+C_S\alpha_{i,j}+C_N\alpha_{i,j-1})u^{n+1}_{i,j}]
\end{aligned}$$

or

$$\begin{aligned}
&u^{n+1}_{i,j} =\\
&\frac{\begin{aligned}[u^n_{i,j}h^2+\mu^{n+1}\tau(C_E\alpha_{i,j}u^n_{i+1,j}+C_W\alpha_{i-1,j}u^n_{i-1,j}\\
+C_S\alpha_{i,j}u^n_{i,j+1}+C_N\alpha_{i,j-1}u^n_{i,j-1})]\end{aligned}}{h^2+\mu^{n+1}\tau(C_E\alpha_{i,j}+C_W\alpha_{i-1,j}+C_S\alpha_{i,j}+C_N\alpha_{i,j-1})}.
\end{aligned}$$

Acknowledgment

The authors would like to thank Rhonda Walcarius from Sunnybrook Health Sciences Centre for performing the MRI scans of the participating subjects. Funding support from GE Healthcare and the Federal Development Agency of Canada is also gratefully acknowledged.

REFERENCES

[1] V. L. Rogers *et al.*, "Heart disease and stroke statistics–2012 update: A report from the American Heart Association," *Circulation*, vol. 125, pp. e2–e220, 2012.

[2] A. C. Lardo, "Real-time magnetic resonance imaging: Diagnostic and interventional applications," *Pediatr Cardiol*, vol. 21, pp. 80–98, 2000.

[3] A. Kolandaivelu, A. C. Lardo, and H. R. Halperin, "Cardiovascular magnetic resonance guided electrophysiology studies," *J. Cardiov. Magn. Reson.*, vol. 11, 2009.

[4] A. P. King, R. Boubertakh, K. S. Rhode, Y. L. Ma, P. Chinchapatnam, G. Gao, T. Tangcharoen, M. Ginks, M. Cooklin, J. S. Gill, D. J. Hawkes, R. S. Razavi, and T. Schaeffter, "A subject-specific technique for respiratory motion correction in image-guided cardiac catheterization procedures," *Med. Imag. Anal.*, vol. 13, pp. 419–431, 2009.

[5] X. Huang, J. Ren, G. Guiraudon, D. Boughner, and T. Peters, "Rapid dynamic image registration of the beating heart for diagnosis and surgical navigation," *IEEE Trans. Med. Imag.*, vol. 28, no. 11, pp. 1802–1814, 2009.

[6] R. Smolíková-Wachowiak, M. P. Wachowiak, A. Fenster, and M. Drangova, "Registration of two-dimensional cardiac images to preprocedural three-dimensional images for interventional applications," *J. Magn. Reson. Imag.*, vol. 22, pp. 219–228, 2005.

[7] Y. L. Ma, G. P. Penney, C. A. Rinaldi, M. Cooklin, R. Razavi, and K. S. Rhode, "Echocardiography to magnetic resonance image registration for use in image-guided cardiac catheterization procedures," *Physics in medicine and biology*, vol. 54, no. 16, p. 5039, 2009.

[8] B. A. Hoffmann, A. Koops, T. Rostock, K. Mullerleile, D. Steven, R. Karst, M. U. Steinke, I. Drewitz, G. Lund, S. Koops, G. Adam, and S. Willems, "Interactive real-time mapping and catheter ablation of the cavotricuspid isthmus guided by magnetic resonance imaging in a porcine model," *European Heart Journal*, vol. 31, pp. 450–456, 2010.

[9] Y. Ma, A. P. King, N. Gogin, G. Gijsbers, C. Rinaldi, J. Gill, R. Razavi, and K. S. Rhode, "Clinical evaluation of respiratory motion compensation for anatomical roadmap guided cardiac electrophysiology procedures," *IEEE Trans. Biomed. Eng.*, vol. 59, no. 1, pp. 122–131, 2012.

[10] A. J. Dick, M. A. Guttman, D. C. P. V. K. Raman, B. S. Pessanha, J. M. Hill, S. Smith, G. Scott, E. R. McVeigh, and R. J. Lederman, "Magnetic resonance fluoroscopy allows targeted delivery of mesenchymal stem cells to infarct borders in swine," *Circulation*, vol. 108, pp. 2899–2904, 2003.

[11] V. Y. Reddy, Z. J. Malchano, G. Holmvang, E. J. Schmidt, A. d'Avila, C. Houghtaling, R. C. Chan, and J. N. Ruskin, "Integration of cardiac magnetic resonance imaging with three-dimensional electroanatomic mapping to guide left ventricular catheter manipulation: feasibility in a porcine model of healed myocardial infarction," *J Am Coll Cardiol*, vol. 44, pp. 2202–2213, 2004.

[12] Z. J. Malchano, P. Neuzil, R. C. Cury, G. Holmvang, J. Weichet, E. J. Schmidt, J. N. Ruskin, and V. Reddy, "Integration of cardiac CT/MR imaging with three- dimensional electroanatomical mapping to guide catheter manipulation in the left atrium: implications for catheter ablation of atrial fibrillation," *J. Cardiovasc. Electr.*, vol. 17, pp. 1221–1229, 2006.

[13] S. R. Dukkipati, R. Mallozzi, E. J. Schmidt, A. d. Godtfred Holmvang, R. Guhde, R. D. Darrow, G. Slavin, M. Fung, Z. Malchano, G. Kampa, J. D. Dando, C. McPherson, T. K. Foo, J. N. Ruskin, C. L. Dumoulin, and V. Y. Reddy, "Electroanatomic mapping of the left ventricle in a porcine model of chronic myocardial infarction with magnetic resonance based catheter tracking," *Circulation*, vol. 118, pp. 853–862, 2008.

[14] K. McLeish, D. Hill, D. Atkinson, J. M. Blackall, and R. Razavi, "A study of the motion and deformation of the heart due to respiration," *IEEE Trans. Med. Imag.*, vol. 21, pp. 1142–1150, 2002.

[15] A. D. Scott, J. Keegan, and D. N. Firmin, "Motion in cardiovascular MR imaging," *Radiology*, vol. 250, no. 2, pp. 331–351, 2009.

[16] B. Fei, J. L. Duerk, D. T. Boll, J. S. Lewin, and D. L. Wilson, "Slice-to-volume registration and its potential application to interventional MRI-guided radio-frequency thermal ablation of prostate cancer," *IEEE Trans. Med. Imag.*, vol. 22, no. 4, pp. 515–525, 2003.

[17] P. Su, J. Yang, K. Lu, N. Yu, S. Wong, and Z. Xue, "A fast CT and CT-fluoroscopy registration algorithm with respiratory motion compensation for image-guided lung intervention," *IEEE Trans. Biomed. Eng.*, vol. 60, no. 7, pp. 2034–2041, 2013.

[18] D. Li, H. Li, H. Wan, J. Chen, G. Gong, H. Wang, L. Wang, and Y. Yin, "Multiscale registration of medical images based on edge preserving scale space with application in image-guided radiation therapy," *Phys. Med. Biol.*, vol. 57, no. 16, pp. 5187–5204, 2012.

[19] D. Paquin, D. Levy, and L. Xing, "Multiscale registration of planning CT and daily cone beam CT images for adaptive radiation therapy," *Med. Phys.*, vol. 36, pp. 4–11, 2009.

[20] T. Mäkelä, P. Clarysse, O. Sipilä, N. Pauna, Q. C. Pham, T. Katila, and I. E. Magnin, "A review of cardiac image registration methods," *IEEE Trans. Med. Imag.*, vol. 21, no. 9, pp. 1011–1021, 2002.

[21] U. E. Aladl, G. A. Hurwitz, D. Dey, D. Levin, M. Drangova, and P. J. Slomka, "Automated image registration of gated cardiac single-photon emission computed tomography and magnetic resonance imaging," *J. Magn. Reson. Imag.*, vol. 19, no. 3, pp. 283–290, 2004.

[22] D. Perperidis, R. H. Mohiaddin, and D. Rueckert, "Spatio-temporal free-form registration of cardiac mr image sequences," *Med. Imag. Anal.*, vol. 9, no. 5, pp. 441–456, 2005.

[23] F. Gigengack, L. Ruthotto, M. Burger, C. H. Wolters, X. Jiang, and K. P. Schafers, "Motion correction in dual gated cardiac pet using mass-preserving image registration," *IEEE Trans. Med. Imag.*, vol. 31, no. 3, pp. 698–712, 2012.

[24] W. Shi, X. Zhuang, H. Wang, S. Duckett, D. V. Luong, C. Tobon-Gomez, K. Tung, P. J. Edwards, K. S. Rhode, R. S. Razavi, *et al.*, "A comprehensive cardiac motion estimation framework using both untagged and 3-D tagged mr images based on nonrigid registration," *IEEE Trans. Med. Imag.*, vol. 31, no. 6, pp. 1263–1275, 2012.

[25] E. Haber and J. Modersitzki, "Beyond mutual information: A simple and robust alternative," in *Bildverarbeitung für die Medizin 2005*, H. Meinzer, H. Handels, A. Horsch, and T. Tolxdorff, Eds. Springer Berlin/ Heidelberg, 2005, pp. 350–354.

[26] P. Thevenaz, U. E. Ruttimann, and M. Unser, "A pyramid approach to subpixel registration based on intensity," *IEEE Trans. Image Process.*, vol. 7, no. 1, pp. 27–41, 1998.

[27] J. Modersitzki, *Numerical Methods for Image Registration*. New York: Oxford University Press, 2004.

[28] L. I. Rudin, S. Osher, and E. Fatemi, "Nonlinear total variation based noise removal algorithms," *Phys. D*, vol. 60, no. 1, pp. 259–268, 1992.

[29] E. Tadmor, S. Nezzar, and L. Vese, "A multiscale image representation using hierarchical (bv, l 2) decompositions," *Multiscale Model. Simul.*, vol. 2, no. 4, pp. 554–579, 2004.

[30] P. Athavale, R. Xu, P. Radau, A. Nachman, and G. Wright, "Multiscale TV flow with applications to fast denoising and registration," in *SPIE Medical Imaging*. International Society for Optics and Photonics, 2013, pp. 86 692K1–86 692K7.

[31] G. Aubert and P. Kornprobst, *Mathematical problems in image processing: partial differential equations and the calculus of variations*. Springer, 2006, vol. 147.

[32] F. Andreu, C. Ballester, V. Caselles, and J. Mazón, "Minimizing total variation flow," *Differential and Integral Equations*, vol. 14, no. 3, pp. 321–360, 2001.

[33] P. Perona and J. Malik, "Scale-space and edge detection using anisotropic diffusion," *IEEE Trans. Pattern Anal. Mach. Intell.*, vol. 12, no. 7, pp. 629–639, 1990.

[34] P. Guidotti, "A new nonlocal nonlinear diffusion of image processing," *Journal of Differential Equations*, vol. 246, no. 12, pp. 4731–4742, 2009.

[35] J. A. Nelder and R. Mead, "A simplex method for function minimization," *The Computer Journal*, vol. 7, pp. 308–313, 1965.

[36] K. H. Zou, S. K. Warfield, A. Bharatha, C. Tempany, M. R. Kaus, S. J. Haker, W. M. Wells III, F. A. Jolesz, and R. Kikinis, "Statistical validation of image segmentation quality based on a spatial overlap index," *Academic Radiology*, vol. 11, no. 2, pp. 178–189, 2004.

[37] T. W. Anderson and D. A. Darling, "A test of goodness of fit," *Journal of the American Statistical Association*, vol. 49, no. 268, pp. 765–769, 1954.

[38] F. Wilcoxon, "Individual comparisons by ranking methods," *Biometrics Bulletin*, vol. 1, no. 6, pp. 80–83, 1945.

[39] G. Shechter, C. Ozturk, J. R. Resar, and E. R. McVeigh, "Respiratory motion of the heart from free breathing coronary angiograms," *IEEE Trans. Med. Imag.*, vol. 23, pp. 1046–1056, 2004.

[40] G.-A. Turgeon, G. Lehmann, G. Guiraudon, M. Drangova, D. Holdsworth, and T. Peters, "2D-3D registration of coronary angiograms for cardiac procedure planning and guidance," *Med. Phys.*, vol. 32, no. 12, pp. 3737–3749, 2005.

[41] R. Membarth, F. Hannig, J. Teich, M. Korner, and W. Eckert, "Frameworks for GPU accelerators: A comprehensive evaluation using 2D/3D image registration," in *Application Specific Processors (SASP), 2011 IEEE 9th Symposium on*. IEEE, 2011, pp. 78–81.

[42] J. McClelland, D. J. Hawkes, T. Schaeffter, and A. P. King, "Respiratory motion models: A review," *Med. Imag. Anal.*, vol. 17, no. 1, pp. 19–42, 2013.